Surface & Coatings Technology 486 (2024) 130831

Contents lists available at ScienceDirect

Surface & Coatings Technology

journal homepage: www.elsevier.com/locate/surfcoat

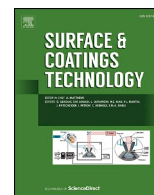

Decoupling inert and reactive gas supply to optimize ion beam sputter deposition apparatus for a more efficient material deposition

Sebastian L. Benz *, Isabel Müller, Angelika Polity, Peter J. Klar, Martin Becker, Sangam Chatterjee

Institute for Exp. Physics I and Center for Materials Research (ZfM/LaMa), Justus Liebig University of Giessen, Germany

ARTICLE INFO

Keywords:
Ion beam sputter deposition
Nickel oxide
Thin films

ABSTRACT

For all technologies, the energy-payback time (EPBT) serves as a critical metric. As an example, we study ion beam sputter deposition (IBSD), a sputter deposition approach where plasma, target, and substrate are decoupled. We compare three different configurations for reactive gas injection in order to demonstrate how the corresponding thin-film deposition processes can be improved, i.e., via the ion source, close to the target, or close to the substrate. The latter two decouple the introduction of inert and reactive gases, thus enabling substantial additional control in the deposition process. We investigate nickel oxide (NiO_x) thin films as a versatile model system which is of interest for a wide range of applications. In the growth process, we vary growth times between 5 and 205 min and examine O_2/Ar flow ratios between 0.13 and 5.82 for the different gas inlet configurations. Based on detailed structural and compositional analyses of the deposited thin films, we show that the deposition mode significantly influences crystal quality, growth rate, and surface roughness. Notably, the configuration where the reactive gas is injected close to the Ni target leads to significant improvement of the crystalline quality of the deposited NiO_x layers for thicknesses of 30–200 nm. Furthermore, reactive gas injection close to the substrate yields films of comparable quality for thicknesses of 800 nm and above, but at almost twice the growth rate. These findings present a promising avenue for optimizing EPBT of IBSD by yielding better films in shorter process times and at less energy consumption. Yet, for low O_2/Ar ratios the formation of a secondary phase of $NiAl_2O_4$ spinel is observed.

1. Introduction

A major hurdle when introducing a novel device is its acceptance by future users. In addition to device performance, aspects of sustainability and environment friendliness of the technology affect the user's decision whether to buy or not to buy a novel device [1,2]. If a new technology is environmentally harmful, it will unlikely replace established solutions just due to better performance. Achieving sustainability in the fabrication of novel devices is hence of paramount importance. It necessitates credible assessments of the environmental impact of the fabrication process. Life cycle assessments from cradle-to-cradle of resource consumption of technologies in terms of energy consumption, carbon footprint, and materials provide quantitative parameters for decision making [3,4]. For example, in case of sustainable energy technologies such as photovoltaic modules the energy payback time (EPBT) describes the period of time a module must operate and turn solar power into electrical power to recover the energy it took to produce the module initially. Thus, the EPBT is such a quantitative measure helping in the decision process [5]. In order to reduce the EPBT of a technology or to improve the sustainability assessment of a device, all stages of its life cycle and use need to be optimized.

Thin-film deposition processes play a major role in device fabrication and are thus at the cradle of the life cycle of most modern devices [6,7]. For example, thin films are the active material in large-scale sustainable energy technologies such as smart windows and solar cells as much as in micro-scale semiconductor devices [8–13]. Various technologies are employed for thin-film deposition comprising physical vapor deposition (PVD) and chemical vapor deposition (CVD) approaches. Typically, these methods have in common to operate under vacuum conditions and often a substrate heating is required to ensure crystallization of the deposited thin films. Both requirements contribute to the energy consumption of the thin-film growth process. Of course, also production

* Corresponding author.
E-mail address: Sebastian.L.Benz@phys.chemie.uni-giessen.de (S.L. Benz).

https://doi.org/10.1016/j.surfcoat.2024.130831
Received 22 December 2023; Received in revised form 18 April 2024; Accepted 23 April 2024
Available online 26 April 2024
0257-8972/© 2024 The Authors. Published by Elsevier B.V. This is an open access article under the CC BY-NC-ND license (http://creativecommons.org/licenses/by-nc-nd/4.0/).

time, that is closely related to the deposition rate is very important in this context. The challenge in further advancement of growth apparatus in terms of a better energy efficiency and thus a shorter EPBT of the fabricated devices is to improve or at least preserve the quality of the deposited thin films. For example, a smaller/cheaper vacuum system may lead to a higher content of impurities in the high vacuum atmosphere and thus may reduce thin film quality. Similarly, reducing the power used for substrate heating may reduce the substrate temperature and result in less crystallinity and, thus, inferior quality of the deposited film. Furthermore, an increase of deposition rate is often not compatible with a better thin-film quality.

Here, we want to present an example of how to improve the growth process of a specific PVD method, i.e. ion beam sputter deposition (IBSD). A decoupling of inert and reactive gas has been demonstrated to increase the growth rate for other sputtering methods, i.e., for magnetron sputter deposition [14]. Here, we want to adapt this promising approach to IBSD and investigate systematically the influence of the injection position of the reactive gas. We choose nickel oxide (NiO_x) as material for our case study. NiO_x has many interesting properties and is a candidate material for many device classes [15–19]. NiO exhibits several key characteristics, including antiferromagnetism, transparency as a p-type semiconductor, and a cubic crystal lattice of rocksalt structure. The band gap energy of NiO is reported to range between 3.25 and 4.5 eV or 2.54 and 4.80 eV [20–24], depending on the method used for its determination and estimation. The Néel temperature is approximately 520 K [24,25]. Due to its physical properties, NiO is considered as a versatile material with a high potential for energy applications [24]. Furthermore, it can be considered sustainable as the two chemical elements Ni and O are available in abundance. Also, it exhibits a very high recovery rate regarding Ni [26]. In addition to the stoichiometric form of NiO, non-stoichiometric NiO_x films are frequently obtained, due to oxygen depletion/excess [27–29]. This behavior is explained by the Ni—O phase diagram, in which an NiO-like phase is formed over a wide range of metal-to-oxygen ratios [30,31]. As a result, NiO serves as an excellent model system for optimizing growth apparatus and processes due to its chemical and compositional simplicity. A comparison in terms of quality with samples grown by other methods is facile, as numerous successful synthesis reports of NiO thin films can be found in literature. Here, different fabrication methods have been employed, including molecular beam epitaxy (MBE) [32], metal-organic chemical vapor deposition (MOCVD) [33], sputtering techniques [34,35], pulsed laser deposition (PLD) [36,37], and electron beam evaporation [38].

2. Experimental details

NiO_x thin films are grown using IBSD on *c*-cut sapphire substrates, employing a 3″ metallic Ni target with a purity of 3N (Kurt J. Lesker Company). The 2″ sapphire substrates are manually cut yielding sample sizes from about 6×6 mm^2 to 8×8 mm^2. Fig. 1 schematically illustrates the setup of the IBSD growth apparatus. We use a radio frequency ion source (referred to as RIT, coming from radiofrequency ion thruster) [39,40] to create the primary ion beam. The ion beam particles bombarding the target (here the Ni target) sputter a plume that consist of a mixture of target material and reaction products such as NiO_x [41,42]. The substrate is closely positioned in the direction of the maximum intensity of this secondary plume coming from the target, and not in line-of-sight with the primary ion beam from the ion source. The oxygen necessary for obtaining the NiO_x layer on the substrate may be provided at different locations between ion source and substrate. First, this may be done via the gas inlet of the ion source, an often-used approach in IBSD [43–45]. In the following, we call this configuration RIT injection configuration. In this configuration, both the inert gas Ar and the reactive gas O_2 are injected into the RIT [42,46,47] and are used to generate the plasma. Subsequently, the plasma ions are extracted and directed towards the target. Second, the so-called (near) target injection configuration is employed. Here, solely Ar is used as working gas inside

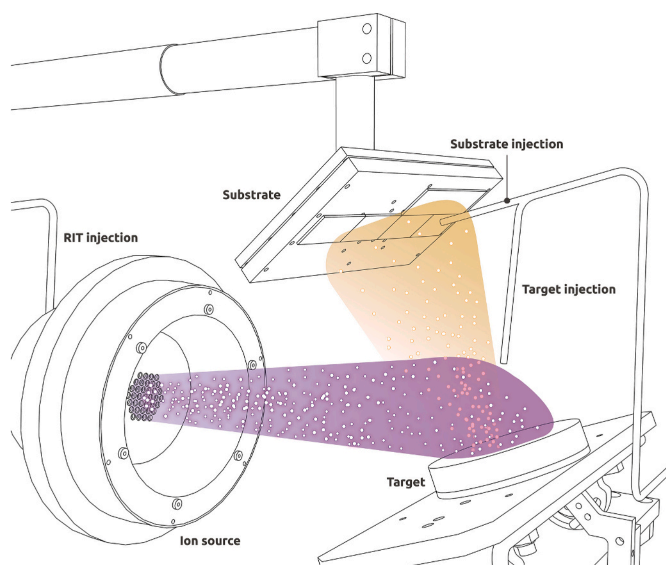

Fig. 1. Schematic illustration of the three different positions for O_2 injection into the IBSD apparatus, namely the RIT injection, the substrate injection and the target injection. Only one injection position is used at a time. RIT injection is shown here.

the ion source, whereas the reactive gas O_2 is directed onto the target through a 1/8″ stainless steel pipe. Third, we use the so-called (near) substrate injection configuration. Here, again solely Ar is used as working gas inside the RIT for generating the plasma, while molecular oxygen is sprayed onto the substrate surface using a 1/8″ stainless steel pipe. This approach of being able to switch between different injection sites of the reactive gas, i.e. of oxygen, is somewhat comparable to meta-mode sputtering, where metal deposition and subsequent oxidization take place at different locations [48]. All injection configurations are illustrated in Fig. 1.

Several sample series are grown employing the different gas injection configurations. Identical partial pressures are used in all injection modes. The flows are selected and controlled with mass flow controllers (*Tylan*, *MKS*) to maintain a constant average background pressure throughout the series for comparison. The pressure is tracked with a full range gauge (*Pfeiffer Vacuum*), obeying correction terms for individual gases. The following values for the O_2/Ar ratio have been studied: 0.13, 0.46, 0.67, 0.91, 1.20, 1.59, 2.79, 5.82. One should note, that the flow ratio and injection mode has a weak influence on the beam diameter only. The beam diameter varies between 5 and 6 cm. In a first series of samples the deposition time is set to 2 h. In a second series, the growth times are equal to 5, 15, 45, 60, 90, 120, 205 min at fixed O_2/Ar ratio of 0.91 for assessing the dependence of the properties on film thickness. Furthermore, a third series, an alloying series, is employed for investigating the impact of Al diffusion from the substrate into the thin films. This becomes necessary, as it is possible to produce a $NiAl_2O_4$ spinel phase at the interface between sapphire substrate and thin film. The Al content is varied by covering the Ni target partially with high purity Al foil (3N). The Al/Ni ratio has been effectively varied between 0.27 and 0.4 this way according to XPS analysis.

The RIT's plasma is operated at 2 MHz with a power of 230 W. The ions are extracted from the ion source with a kinetic energy of 2400 eV. To ensure temperature equilibrium during the growth process, the *c*-cut sapphire substrates are pre-heated to 550 °C. The coil of the RIT and the target are water cooled during operation. Other parts remain at room temperature. The base pressure of the system without providing working gas is better than 2×10^{-6} mbar. The total flow of oxygen and argon independent of the chosen flow ratio yields an average background pressure of 5×10^{-4} mbar. The distance between RIT and target is 0.2 m, that between target and substrate is 0.1 m. The target is pre-sputtered for

30 min prior to starting the actual deposition process in order to remove residual contaminants under process conditions.

We comprehensively characterize the grown layers in terms of their structural and compositional properties. For this purpose, we employ X-ray diffraction (XRD), atomic force microscopy (AFM), and X-ray photoelectron spectroscopy (XPS). The crystallinity of the sputtered NiO_x thin films is investigated using XRD in Bragg-Brentano geometry, employing a Siemens D5000 diffractometer. The same device is used for X-ray reflectometry (XRR) measurements that provide film thicknesses and, taking into account the deposition time, the corresponding growth rates. The growth rate determined is used to extrapolate the thickness of films that exceed the maximum thickness where XRR is applicable. If growth rate determination and direct thickness measurements via XRR are not possible, ellipsometry measurements are conducted between 400 and 1000 nm. Morphological analysis is performed for selected samples (O_2/Ar ratios: 0.46, 0.91, 1.20, 1.59, 5.82) using a Zeiss Merlin scanning electron microscope (SEM) and a Bruker Multimode 8 atomic force microscope (AFM) operating in tapping mode with a silicon nitride tip. AFM data are evaluated using Nanoscope 9.2 (Bruker) software and Gwyddion software [49]. XPS measurements are conducted using a Phi VersaProbe II apparatus for determining the atomic fractions of O and Ni in the thin films. A pass energy of 23.5 eV is set for measuring detail spectra of O 1*s*, C 1s and Ni 2p core levels, resulting in a spectral resolution of 0.2 eV. Survey scans are conducted with a pass energy of 93.9 eV and a resolution of 0.8 eV. Samples are exposed to an Ar^+ beam with an acceleration of 1 kV for 180 s to clean the surface from possible contaminants which may be collected during transport through air. Excitation is provided by a monochromatic Al Kα source (1486.6 eV). Charge neutralization is achieved by combining a flux of e^- and Ar^+ ions. The binding energy axis is post-calibrated to the signal of adventitious carbon (284.8 eV). The relative concentrations X_s of each element are calculated after correcting for the chemical sensitivity (using tabulated relative sensitivity factors RSF_s of the XPS instruments manufacturer for signal *s*) and apparatus response (transmission function *T(E)*):

$$X_s = \frac{100\,A_i}{\sum_j A_j},$$

where the intensity correction is contained in

$$A_s = \frac{I_s}{T(E)\,\lambda\,RSF_s},$$

where I_s and λ are the measured intensity of the signal *s* and the correction for differences in emergence path length, respectively. A background correction is applied using a Shirley-background [50]. For the determination of relative concentrations, deconvolution of spectra is not necessary. The area between raw signal and background yields the intensity I_s.

3. Results and discussion

We employ XRD in Bragg-Brentano geometry for assessing the crystallographic structure of the thin films. Wide-angle survey scans (not shown here) are dominated by strong signals of the sapphire substrate and signals in the angular range where the (111) signal of rocksalt NiO is expected (37.249° according to PDF# 00-044-1159). Fig. 2 shows three series of XRD θ-2θ scans in this angular range of thin films deposited at different O_2/Ar flow ratios. Each series corresponds to one of the three different configurations for oxygen injection during the growth process. The results obtained on samples grown in the RIT injection configuration are shown in graph (a), those of samples fabricated in the target injection configuration in graph (b), and those of samples synthesized in the substrate injection configuration in graph (c). All three series of XRD traces exhibit similar trends almost independent of the site of oxygen injection. For the lowest O_2/Ar flow ratio investigated in this study (0.13) almost no XRD reflection is observed in case of the RIT injection mode. Slightly stronger signals are present for this flow ratio for thin films prepared by the other two injection modes, i.e., target injection mode and substrate injection mode. Probably, the amount of oxygen available is not sufficient to form NiO_x in case of the RIT injection configuration, but at the same time too high to form the metallic phase. In case of the other two injection configurations, the available amount of oxygen is already sufficient to form the NiO_x phase and crystallization of this phase is observed. However, a more efficient crystallization sets in at higher O_2/Ar flow ratios. In particular, the NiO (111) reflection tends to shift towards its bulk value (dashed vertical line) with an increase of the O_2/Ar flow ratio. This suggests that lower O_2/Ar flow ratios yield sub-stoichiometric material and stoichiometric nickel(II) oxide is obtained at the highest O_2/Ar flow ratio only. One should note, that the change in crystallinity may also be attributed to a change in film thickness, as the film thickness diminishes with increasing O_2/Ar flow ratios (see also contents S8-S10 in SI). It has been shown, that crystallization properties are influenced by the film thickness [51]. Exemplarily, the diffraction curve of a stoichiometric NiO thin film deposited in the RIT injection configuration is shown in Fig. 2(d). The corresponding rocking curve exhibits a full-width-at half-maximum (FWHM)

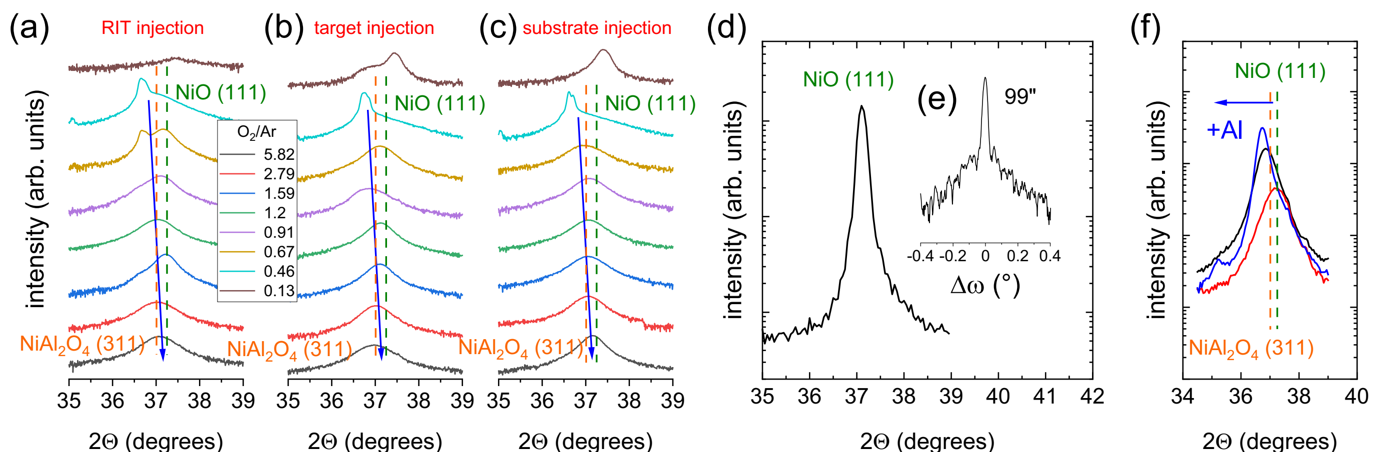

Fig. 2. X-ray diffraction measurements of thin films deposited in RIT injection configuration (a), target injection configuration (b), and substrate injection configuration (c). All measurements are performed in Bragg-Brentano geometry. The data has been shifted for clarity. The O_2/Ar flow ratio used in each deposition process is given in the legend. (d) X-ray diffraction measurement of the NiO thin film obtained in the RIT injection series at the highest O_2/Ar ratio employed, and its corresponding rocking curve (e). X-ray diffraction measurements of samples of the NiO – Al alloying series with three different ratios of Al/Ni of 0.27 (red), 0.38 (black), and 0.4 (blue) (f). The discussion of the film thicknesses can be found in contents S8 – S10 in the SI.

as small as 99 arcsec, cf. Fig. 2(e). This value is <50 % of values observed in conventional sputtering, e.g., 216 arcsec [35]. The FWHM value of our NiO thin film can well compete with FWHM values of NiO thin films grown by other methods or on other substrates [32–34,37]. However, the rocking curve's FWHM alone cannot serve as a criterion for sample quality as it also depends on film thickness, as we will discuss below.

Another feature common for all three oxygen injection modes is the remarkably high crystallinity of the layers obtained at low oxygen flows as shown by the high intensity reflection at around 36.5° in the X-ray patterns (cf. Fig. 2a–c). This reflection manifests itself already at very short deposition times, i.e. very low film thicknesses (cf. Fig. S1). We do not attribute this feature to NiO_x but rather to the formation of a $NiAl_2O_4$ spinel phase. Most likely, this phase is formed at the interface between the sapphire substrate and the thin film, as observed also for other material systems [52]. We studied the third series of samples, the alloying series, where Al is added during the growth process, as described in the previous section, to further corroborate the aforementioned analysis. The X-ray patterns for three samples of this series with ratios of Al/Ni of 0.27, 0.38, and 0.4 (cf. Fig. 2(f)) reveal that with higher Al/Ni ratio, i.e., higher Al content, the NiO_xAl_y reflection shifts towards the 2Θ angle of the (311) reflection of the $NiAl_2O_4$ spinel phase (37.010° according to PDF# 00-010-0339).

To further verify the assumption that the thin films are sub-stoichiometric NiO_x at O_2/Ar ratios of <5.82, we employ XPS to obtain the O/Ni ratio in our thin films. The results are depicted in Fig. 3. The survey scans do not reveal unexpected impurities, cf. Fig. 3(a). To determine the exact composition, detail spectra are evaluated to determine reliable results [53]. Exemplarily, detail spectra of Ni $2p_{3/2}$ (b) and O 1*s* (c) core level after 180 s of Ar^+ irradiation, respectively, are shown. Besides the expected NiO signals marked in blue, the spectra show Ni related features [54]. On the one hand, the Ni signals show satellites towards higher binding energy [55–57]. On the other hand, the Ar^+ beam is not only sputtering material from the surfaces but also damages the material below to some extent. Thus, material is reduced which evokes signals on the lower binding energy side. Nonetheless, the overall trends in composition variation are preserved (see also Discussion S5 in SI). Potential preferential sputtering is not promoted by undesired impurities and, hence, should have the same effect for all samples. Furthermore, matrix effects are highly unlikely, as the lattices of the thin films are quite comparable as discussed earlier. For clarity, we show the composition values as O/Ni ratio in Fig. 3(d). Similar to the XRD results, the films at very low O_2/Ar flow do not seem to follow the trends observed for the rest of the thin film series. The low oxygen flow regime yields metal-rich films. Surprisingly, the composition of the film of the RIT injection series, that does not show crystallization in XRD, lies in between those of the other two injection modes for the lowest O_2/Ar flow. An increasing oxygen flow shifts the O/Ni ratio in the film towards 1:1. Hence, the composition results corroborate the trends derived from the XRD data, i.e., stoichiometric NiO thin films are obtained at the highest relative O_2 flow (O_2/Ar ratio of 5.92) investigated in this study independent of the oxygen injection mode.

We examined the NiO_x thin-film surfaces by AFM in order to assess the surface morphology. Changes in surface morphology may be induced by a variation of stoichiometry which in turn may be reflected by different grain growth. In Fig. 4 and Fig. S2 (SI), we present corresponding results for selected samples of the three injection mode series. The thin films deposited at the lowest O_2/Ar flow ratio (i.e. the films in the first column) show very smooth surfaces independent of the O_2 injection configuration. It is remarkable, that the thin films synthesized at these low O_2/Ar ratios do not follow the general trends observed for the rest of the series. This holds independent of the three gas injection configurations applied. Furthermore, the surface of the sample of the RIT injection series grown at the lowest O_2/Ar flow ratio exhibits additional needle-like pillars. These pillar-like structures may be an explanation, why no crystallization can be observed for this film, i.e., the mixed structure of a smooth film on the one hand and the pillar-like growth on the other hand seem to hamper crystallization. At higher O_2/Ar ratios, the situation is different. The AFM images of the film surfaces consist of many small features comparable in size with the pillars on the surface of the sample of the RIT injection series grown at the lowest O_2/Ar flow ratio. We tentatively attribute these features to small grains separated by grain boundaries. The resolution of AFM approaches its limits when detecting these features. However, the structure becomes easier accessible with an SEM (cf. Fig. S3). Triangular patterns

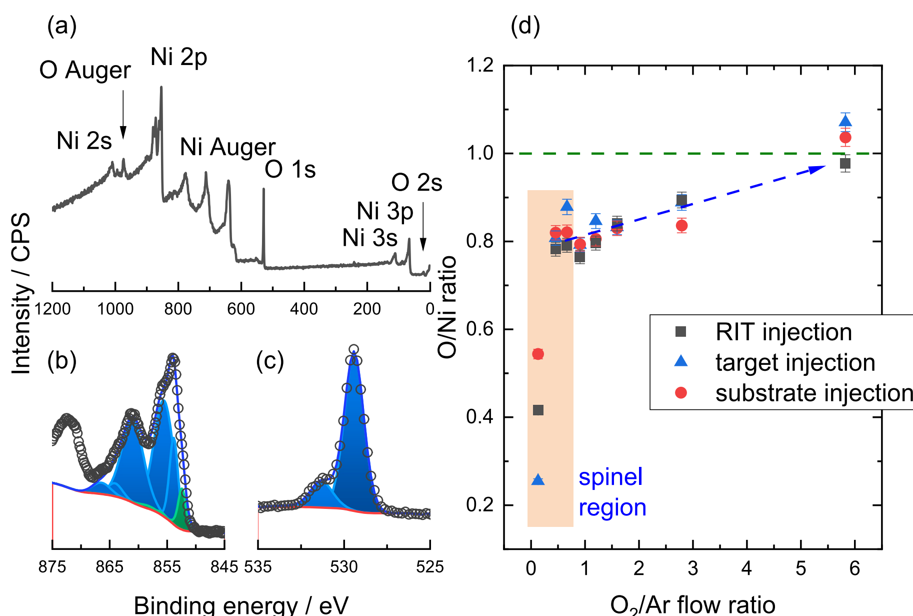

Fig. 3. Typical XPS measurements after Ar^+ irradiation: Survey spectrum (a) and detail spectra of Ni $2p_{3/2}$ (b) and O 1*s* (c) core levels are fitted according to Biesinger et al. [54]. NiO components are marked in blue, while Ni signals are indicated in green. The area between the dark blue line and the background is taken into account for the O/Ni ratio determination. In red, the calculated Shirley background is displayed. (d) The composition of the thin films determined by XPS after surface cleaning by Ar ion beam etching. The region of flow ratios where films reveal the spinel-related reflection in XRD is marked. The ratio of Ni to O in stoichiometric NiO is shown as a horizontal reference line.

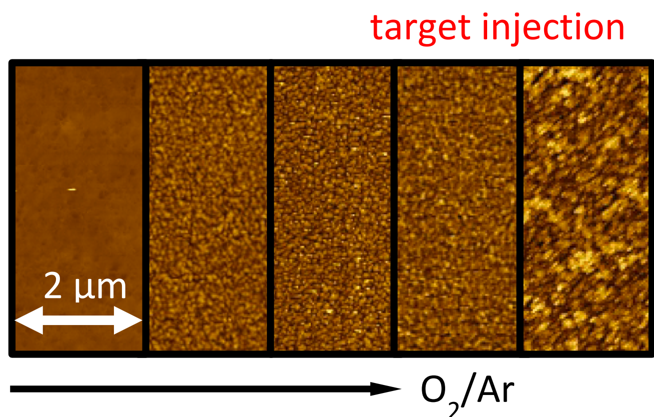

Fig. 4. Atomic force microscopy images of the surface for selected sample of the target injection series and increasing O_2/Ar flow ratio. Corresponding images for RIT injection as well as substrate injection can be found in Fig. S2 of the SI. Additional information on roughness, pit-to-valley distances and the color scale span can be found in Table S7 of SI.

at the grain boundaries can be observed very clearly at high magnifications with the SEM. Such triangular shapes have been also observed in earlier studies by scanning electron microscopy (SEM) in case of thin films grown in a RIT injection mode [42]. The presence of these features has been considered an indicator of bi-domain growth. At the highest O_2/Ar ratio used here, agglomeration of grains to bigger structural features takes place. While the roughness decreases for RIT injection and substrate injection, an increased roughness and significantly bigger agglomerates are found in case of target injection. Very likely, this has to do with a decreased secondary particle kinetic energy. With increasing oxygen flow, the local density of O_2 molecules in front of the target is increased. This leads to higher scattering probability of the Ar^+ ions with the O_2 molecules. During the scattering process, kinetic energy from Ar^+ ions is transferred to crack the O_2 molecules and excite the atoms. Thus, the Ar^+ ions of the beam are slowed down more than in the other two modes prior to impinging on the target surface. Hence, the energy of the sputtered particles is also lowered, as their kinetic energy is dependent on the kinetic energy of the impinging ions [44,58]. Despite the non-equilibrium situation, if one followed the line of arguments by Wulff for surface reconstruction in thermal equilibrium, this would lead to shorter diffusion lengths and thus bigger agglomerates on the surface [59,60]. One should note that there may also be a slowing down of the sputtered material between target and substrate in the case of substrate injection. Still, it seems that its impact is not as severe, as, in this case, films show generally a smaller roughness.

It is well known, that thin-film properties strongly depend on the thickness of the deposited film. This also holds true for NiO_x [61–63]. Therefore, we will focus on three series of samples of different thickness, i.e., grown with different deposition times, one series for each inlet position. As it is our goal to optimize thin film growth towards the minimization of the EPBT, a high growth rate is desirable for two reasons. First, it minimizes the production time and, second, it reduces energy consumption, e.g., due to substrate heating (which is often essential to promote crystallinity of the deposited film), running the vacuum system and the ion source, etc. In general, the deposition rate in the sputtering process decreases with a higher oxygen content in the plasma [64–66]. However, it needs to exceed a certain threshold in our process in order to suppress the undesired spinel formation at the interface. In consequence, we choose the O_2/Ar ratio of 0.91. The first series has shown that this value is the lowest O_2/Ar ratio where the parasitic spinel phase is not present. Hence, we do not expect an influence of the spinel phase on the results discussed in what follows. We selected deposition times of 5, 15, 45, 60, 90, 120, and 205 min in the film deposition processes of each series. Fig. 5 shows the FWHM values of the rocking curve of the main peak of the deposited films in dependence on deposition time (a) and on the layer thickness (b). The FWHM is smallest for the films grown in target injection mode, while the other two injection modes yield similar, but larger values. This finding is independent of the abscissa, i.e., regardless whether the FWHM values are plotted as function of the actual layer thickness or of the deposition time. The FWHM values of all three injection modes converge for layer thicknesses larger than 800 nm, mainly due to a steep increase of the FWHM in the target injection mode series. Notably, the RMS roughness of the film surfaces as obtained by AFM, cf. Fig. 5(c), yields comparable results for the three series of samples. However, the deposition rate is highly dependent on the injection mode used. We find the following behavior of the growth rates: substrate injection mode (4.95 nm/min) > target injection mode (3.71 nm/min) > RIT injection mode (3.39 nm/min). We propose the following explanation for the order of growth rates found. The mean free path of Ar at room temperature inside the IBSD apparatus is 4 m and 0.2 m at its average base pressure ($<2 \times 10^{-6}$) mbar) and working pressure (ca. 5×10^{-4} mbar), respectively. In both cases, it is longer or comparable to the relevant geometric distances between ion source - target and target - substrate of 0.2 and 0.1 m, respectively. Thus, considerable scattering of Ar ions of the primary beam or particles of the secondary plume is only expected close to the O_2 inlet where locally the pressure is higher than average. In case of substrate injection, pure Ar is used to sputter from a metallic target. Ar is a more efficient projectile for Ni sputtering than O as the energy transfer from projectile ion to target atom is best for comparable masses (A_U(Ni) $\approx$ 58.7, A_U(Ar) $\approx$ 40, A_U(O) $\approx$ 16). It should also be mentioned that the theoretical sputter yield Y is much higher, if Ar will is used as projectile instead of O ($Y_{\mathrm{Ni,O}} \approx 1.187$; $Y_{\mathrm{Ni,Ar}} \approx 2.513$) [67]. Furthermore, the oxidation of sputtered metal occurs efficiently close to the substrate where O_2 is injected, resulting in the highest growth rate. In target injection mode, less metal is sputtered. Here, the density of O_2 molecules is the highest in front of the target, while it is highest at the substrate for substrate injection. Hence, for substrate injection, the Ar^+ ions impinge directly on the target surface and sputter material off the target, whereas the Ar^+ ions have to move through a "barrier" of O_2 molecules before reaching the target in case of target injection. During the scattering processes, the Ar^+ ions are slowed down as described earlier. Thus, the Ar^+ ions are slower in target injection when they interact with the target surface compared to substrate injection. Thus, slowed down, less Ni is sputtered than in substrate injection mode. Furthermore, one should also consider the oxidation of the target's surface. In case of substrate injection virtually no oxide layer is present on the Ni surface due to the elongated pre-sputtering prior to the film deposition. Contrary to this, a significant amount of reactive oxygen species is available in front of the target for the target injection. Clearly, the Ni target will react with the present O species and form NiO_x on the surface. Most likely, such an oxide layer on the surface of the target will reduce the sputtering yield and thus the growth rate. In case of the RIT injection mode, the ion beam consists of both, O^+ and Ar^+ ions. Substantial part of the energy spent in running the plasma is used to crack O_2 molecules inside the plasma vessel [42]. Hence, less material is sputtered from the target as the ion beam consists of Ar ions and atomic O ions yielding an even lower Ni sputtering rate considering the momentum transfer during sputtering. It is also likely, that especially for RIT injection and target injection an NiO_x surface layer is formed during the growth which will reduce the total sputtering rate of the target in this case as well.

Careful analysis of the results obtained by characterizing the three series of NiO samples corresponding the three different injection modes allows us to draw several conclusions. Most importantly, we are able to grow thin NiO films of a desired thickness in the range between 30 and 200 nm with significantly lower FWHM of the rocking curves at the same film thickness in the target injection mode than in the other two injection modes. The FWHM in target injection mode is up to 4 times smaller for thin films with thicknesses between 30 and 200 nm. Keeping in mind,

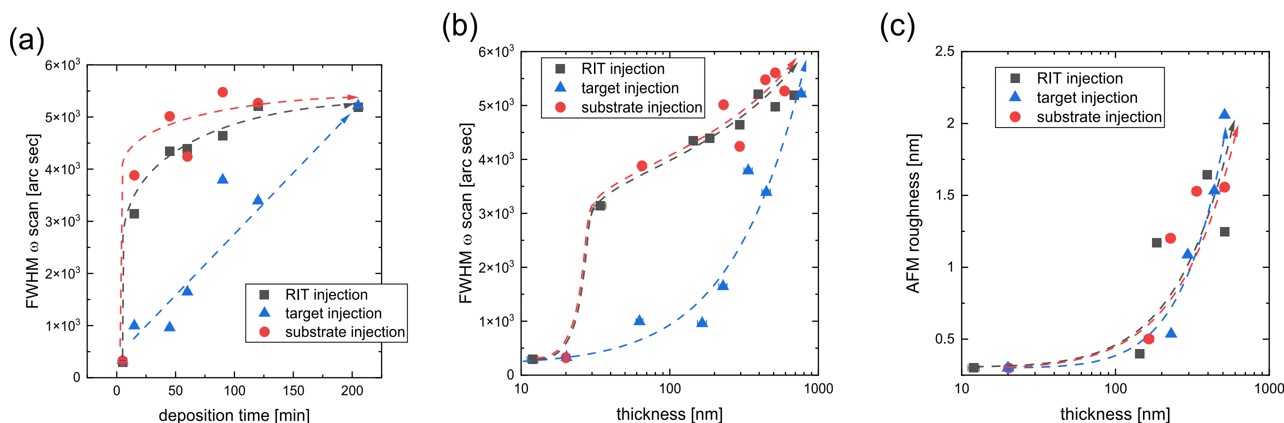

Fig. 5. The FWHM of the XRD rocking curve of the main peak versus deposition time (a) as well as versus corresponding film thickness (b) of samples of different thickness deposited in the three different O_2 inlet configurations, and (c) the AFM roughness of the same thin films plotted versus their thickness. The dashed lines serve as a guide to the eye. The O_2/Ar flow ratio used equals 0.91.

that elevated heating/higher substrate temperatures are often used to promote crystallization [68], this implies that it is possible to achieve a required FWHM of the rocking curve of a thin NiO film with a lower substrate temperature in target injection mode than in the other two modes. Furthermore, the growth rate in target injection mode is about 10 % higher than in conventional RIT injection mode. Thus, it also cuts down the amount of time needed for the growth of a given film thickness compared to the conventional growth approach. Thus, thin film quality and process time are optimized simultaneously by using the target injection mode for films in the range of 30 to 200 nm. For NiO films thicker than 800 nm, the differences in quality of thin films deposited with the three injection modes characterized by FWHM of the rocking curve for the given thickness vanish, making the growth rate the dominant parameter for optimizing the energy efficiency of the growth process. In this case, the substrate injection mode is the best choice. In general, a reconfiguration of the growth apparatus can make the growth process significantly more energy efficient and reduce its EPBT considerably.

We also want to point out additional advantages that target and substrate injection of reactive O_2 gas offer compared with RIT injection. An important parameter for the evaluation for an ion source for material processing is its lifetime. In particular, the grid system of the ion source is exposed to wear and erosion [69]. As the RIT was originally designed for operating with noble gases such as Xe and Ar, a higher erosion of the grids system is expected when a fraction of the working gas is O_2 in RIT injection mode. Thus, utilizing either substrate injection or target injection to provide O for the growth process will also increase the lifetime of the grid system.

4. Conclusion

In conclusion, our study demonstrates the successful growth and characterization of NiO_x thin films using different O_2 injection configurations in the ion beam sputter deposition apparatus. By decoupling the inlets of inert working gas and reactive gas, we are able to significantly influence the deposition parameters. The choice of injection mode affects the growth rate, the crystallinity, and the surface roughness of the deposited thin films. Comparing the substrate injection mode with the conventional RIT injection mode and an alternative target injection mode, we observe a fourfold reduction in the full-width-at-half-maximum (FWHM) of rocking curves for thin films with thicknesses of about 30 to 200 nm deposited in the target injection configuration. For film thicknesses around 800 nm, the dependence of the crystal quality on the injection mode virtually disappears. Still, the crystal quality of all films is highly competitive with the results of other reports. It remains to be noted that the growth rate can be increased by 46 % for these larger film thicknesses by choosing substrate injection instead of the conventional RIT injection mode. These findings open up new possibilities for optimizing the ion beam sputter deposition process, by reducing process times while keeping or even improving the quality of the deposited thin films. Specifically, the energy payback time (EPBT) may be lowered, making our results highly relevant for the IBS deposition of thin films employable in various applications. Our results should remain valid on upscaling of the IBSD apparatus. Therefore, it makes sense for suppliers and users to foresee several inlet sites along the path from ion source via target to substrate for injecting reactive process gases into their IBDS apparatus as there is not one best site for process gas injection. The best position for process gas injection varies with the thin film material to be deposited as well as with its thickness. Thus, process optimization in terms of quality and EPBT requires a flexibility with respect to reactive process gas injection. In the future, we plan to explore the impact of different reactive gas inlet configurations on the growth of other thin-film materials of interest such as other metal oxides, metal nitrides or even oxynitrides.

CRediT authorship contribution statement

Sebastian L. Benz: Writing – review & editing, Writing – original draft, Visualization, Validation, Methodology, Investigation, Formal analysis, Data curation, Conceptualization. **Isabel Müller:** Investigation, Data curation. **Angelika Polity:** Writing – review & editing, Validation, Supervision, Resources, Funding acquisition. **Peter J. Klar:** Writing – review & editing, Supervision, Resources, Project administration, Funding acquisition. **Martin Becker:** Writing – original draft, Investigation, Data curation, Conceptualization. **Sangam Chatterjee:** Writing – review & editing, Supervision, Resources, Project administration, Funding acquisition.

Declaration of competing interest

The authors declare that they have no known competing financial interests or personal relationships that could have appeared to influence the work reported in this paper.

Data availability

Data will be made available on request.

Acknowledgements

We are grateful for funding by the Deutsche Forschungsgemeinschaft in the framework of Research Training Group 2204 “Substitute Materials for Sustainable Energy Technologies” as well as for ERDF funding of the

State of Hesse in the framework of the Innovation Laboratory "High Performance Materials".

The authors thank Elisa Monte for assistance in the preparation of the graphical material. We thank Marius Müller for the fruitful discussion of the ellipsometry results.

Appendix A. Supplementary data

Supplementary data to this article can be found online at https://doi.org/10.1016/j.surfcoat.2024.130831.

References

[1] G. Assefa, B. Frostell, Social sustainability and social acceptance in technology assessment: a case study of energy technologies, Technol. Soc. 29 (2007) 63–78, https://doi.org/10.1016/j.techsoc.2006.10.007.

[2] K. Ek, Public and private attitudes towards "green" electricity: the case of Swedish wind power, Energy Policy 33 (2005) 1677–1689, https://doi.org/10.1016/j.enpol.2004.02.005.

[3] C.K. Chau, T.M. Leung, W.Y. Ng, A review on life cycle assessment, life cycle energy assessment and life cycle carbon emissions assessment on buildings, Appl. Energy 143 (2015) 395–413, https://doi.org/10.1016/j.apenergy.2015.01.023.

[4] G. Finnveden, M.Z. Hauschild, T. Ekvall, J. Guinée, R. Heijungs, S. Hellweg, A. Koehler, D. Pennington, S. Suh, Recent developments in life cycle assessment, J. Environ. Manage. 91 (2009) 1–21, https://doi.org/10.1016/j.jenvman.2009.06.018.

[5] Handbook of Energy Efficiency in Buildings, Elsevier, 2019.

[6] F. Catania, H. de Souza Oliveira, P. Lugoda, G. Cantarella, N. Münzenrieder, Thin-film electronics on active substrates: review of materials, technologies and applications, J. Phys. D Appl. Phys. 55 (2022) 323002, https://doi.org/10.1088/1361-6463/ac6af4.

[7] A.H. Elsheikh, S.W. Sharshir, M.K. Ahmed Ali, J. Shaibo, E.M. Edreis, T. Abdelhamid, C. Du, Z. Haiou, Thin film technology for solar steam generation: a new dawn, Sol. Energy 177 (2019) 561–575, https://doi.org/10.1016/j.solener.2018.11.058.

[8] M. Kamalisarvestani, R. Saidur, S. Mekhilef, F.S. Javadi, Performance, materials and coating technologies of thermochromic thin films on smart windows, Renew. Sustain. Energy Rev. 26 (2013) 353–364, https://doi.org/10.1016/j.rser.2013.05.038.

[9] X. Zhao, J. Guan, J. Li, X. Li, H. Wang, P. Huo, Y. Yan, CeO2/3D g-C3N4 heterojunction deposited with Pt cocatalyst for enhanced photocatalytic CO2 reduction, Appl. Surf. Sci. 537 (2021) 147891, https://doi.org/10.1016/j.apsusc.2020.147891.

[10] A. Vazhayil, L. Vazhayal, J. Thomas, S. Ashok C, N. Thomas, A comprehensive review on the recent developments in transition metal-based electrocatalysts for oxygen evolution reaction, Applied Surface Science Advances 6 (2021) 100184, https://doi.org/10.1016/j.apsadv.2021.100184.

[11] M. Liu, N. Yan, C. Zhang, L. Li, Integrated solar cells with non-toxic inorganic nanocrystals and polymer bulk heterojunction, Applied Surface Science Advances 3 (2021) 100052, https://doi.org/10.1016/j.apsadv.2020.100052.

[12] A. Ashina, R.K. Battula, E. Ramasamy, N. Chundi, S. Sakthivel, G. Veerappan, Dip coated SnO2 film as electron transport layer for low temperature processed planar perovskite solar cells, Applied Surface Science Advances 4 (2021) 100066, https://doi.org/10.1016/j.apsadv.2021.100066.

[13] B.C. Marupalli, T. Adhikary, B.P. Sahu, R. Mitra, S. Aich, Effect of annealing temperature on microstructure and mechanical response of sputter deposited Ti-Zr-Mo high temperature shape memory alloy thin films, Applied Surface Science Advances 6 (2021) 100137, https://doi.org/10.1016/j.apsadv.2021.100137.

[14] S. Schiller, U. Heisig, K. Steinfelder, J. Strümpfel, Reactive D.C. sputtering with the magnetron-plasmatron for tantalum pentoxide and titanium dioxide films, Thin Solid Films 63 (1979) 369–375, https://doi.org/10.1016/0040-6090(79)90042-7.

[15] A.S. Agnihotri, A. Varghese, N. M, Transition metal oxides in electrochemical and bio sensing: a state-of-art review, Applied Surface Science Advances 4 (2021) 100072, https://doi.org/10.1016/j.apsadv.2021.100072.

[16] T.P. Mokoena, H.C. Swart, K.T. Hillie, Z.P. Tshabalala, M. Jozela, J. Tshilongo, D. E. Motaung, Enhanced propanol gas sensing performance of p-type NiO gas sensor induced by exceptionally large surface area and crystallinity, Appl. Surf. Sci. 571 (2022) 151121, https://doi.org/10.1016/j.apsusc.2021.151121.

[17] M. Ullah, H. Lv, Z. Liu, X. Bai, J. Chen, Y. Zhang, J. Wang, B. Sun, L. Li, K. Shi, Rational fabrication of a g-C3N4/NiO hierarchical nanocomposite with a large surface area for the effective detection of NO2 gas at room temperature, Appl. Surf. Sci. 550 (2021) 149368, https://doi.org/10.1016/j.apsusc.2021.149368.

[18] C. Huang, C. Hao, W. Zheng, S. Zhou, L. Yang, X. Wang, C. Jiang, L. Zhu, Synthesis of polyaniline/nickel oxide/sulfonated graphene ternary composite for all-solid-state asymmetric supercapacitor, Appl. Surf. Sci. 505 (2020) 144589, https://doi.org/10.1016/j.apsusc.2019.144589.

[19] U.T. Nakate, R. Ahmad, P. Patil, Y.T. Yu, Y.-B. Hahn, Ultra thin NiO nanosheets for high performance hydrogen gas sensor device, Appl. Surf. Sci. 506 (2020) 144971, https://doi.org/10.1016/j.apsusc.2019.144971.

[20] A.B. Kunz, Electronic structure of NiO, J. Phys. C Solid State Phys. 14 (1981) L455–L460, https://doi.org/10.1088/0022-3719/14/16/001.

[21] A. Svane, O. Gunnarsson, Transition-metal oxides in the self-interaction-corrected density-functional formalism, Phys. Rev. Lett. 65 (1990) 1148–1151, https://doi.org/10.1103/physrevlett.65.1148.

[22] A.J. Varkey, A.F. Fort, Solution growth technique for deposition of nickel oxide thin films, Thin Solid Films 235 (1993) 47–50, https://doi.org/10.1016/0040-6090(93)90241-g.

[23] K. Nama Manjunatha, S. Paul, Investigation of optical properties of nickel oxide thin films deposited on different substrates, Appl. Surf. Sci. 352 (2015) 10–15, https://doi.org/10.1016/j.apsusc.2015.03.092.

[24] J.A. Spencer, A.L. Mock, A.G. Jacobs, M. Schubert, Y. Zhang, M.J. Tadjer, A review of band structure and material properties of transparent conducting and semiconducting oxides: Ga2O3, Al2O3, In2O3, ZnO, SnO2, CdO, NiO, CuO, and Sc2O3, Appl. Phys. Rev. 9 (2022) 011315, https://doi.org/10.1063/5.0078037.

[25] M.S. Seehra, T.M. Giebultowicz, Magnetic structures of fcc systems with nearest-neighbor and next-nearest-neighbor exchange interactions, Phys. Rev. B Condens. Matter 38 (1988) 11898–11900, https://doi.org/10.1103/physrevb.38.11898.

[26] N.M. Al-Mansi, M.N.M. Abdel, Recovery of nickel oxide from spent catalyst, Waste Manag. 22 (2002) 85–90, https://doi.org/10.1016/S0956-053X(01)00024-1.

[27] Y. Lu, W. Hwang, J. Yang, Effects of substrate temperature on the resistivity of non-stoichiometric sputtered NiOx films, Surf. Coat. Technol. 155 (2002) 231–235, https://doi.org/10.1016/s0257-8972(02)00037-3.

[28] S. Oswald, W. Brückner, XPS depth profile analysis of non-stoichiometric NiO films, Surf. Interface Anal. 36 (2004) 17–22, https://doi.org/10.1002/sia.1640.

[29] M. Wang, Y. Thimont, L. Presmanes, X. Diao, A. Barnabé, The effect of the oxygen ratio control of DC reactive magnetron sputtering on as-deposited non stoichiometric NiO thin films, Appl. Surf. Sci. 419 (2017) 795–801, https://doi.org/10.1016/j.apsusc.2017.05.095.

[30] T.B. Massalski, Binary Alloy Phase Diagrams [second print.],, American Society for Metals, Metals Park, Ohio, 1987.

[31] T.B. Massalski, Binary Alloy Phase Diagrams, second. ed, ASM International, Materials Park, Ohio, 1992 second. print,.

[32] M. Budde, T. Remmele, C. Tschammer, J. Feldl, P. Franz, J. Lähnemann, Z. Cheng, M. Hanke, M. Ramsteiner, M. Albrecht, O. Bierwagen, Plasma-assisted molecular beam epitaxy of NiO on GaN(00.1), J. Appl. Phys. 127 (2020) 015306, https://doi.org/10.1063/1.5129881.

[33] T.M. Roffi, S. Nozaki, K. Uchida, Growth mechanism of single-crystalline NiO thin films grown by metal organic chemical vapor deposition, J. Cryst. Growth 451 (2016) 57–64, https://doi.org/10.1016/j.jcrysgro.2016.06.047.

[34] V.A. Luzanov, Growth of thin epitaxial NiO films on LiNbO3 substrates, J. Commun. Technol. Electron. 65 (2020) 1422–1424, https://doi.org/10.1134/s106422692011011x.

[35] K. Nishimoto, K. Shima, S.F. Chichibu, M. Sugiyama, Reactive RF magnetron sputtering epitaxy of NiO thin films on (0001) sapphire and (100) MgO substrates, Jpn. J. Appl. Phys. 61 (2022) 25505, https://doi.org/10.35848/1347-4065/ac4392.

[36] M. Tanaka, M. Mukai, Y. Fujimori, M. Kondoh, Y. Tasaka, H. Baba, S. Usami, Transition metal oxide films prepared by pulsed laser deposition for atomic beam detection, Thin Solid Films 281-282 (1996) 453–456, https://doi.org/10.1016/0040-6090(96)08673-7.

[37] S.D. Singh, A. Das, R.S. Ajimsha, M.N. Singh, A. Upadhyay, R. Kamparath, C. Mukherjee, P. Misra, S.K. Rai, A.K. Sinha, T. Ganguli, Studies on structural and optical properties of pulsed laser deposited NiO thin films under varying deposition parameters, Mater. Sci. Semicond. Process. 66 (2017) 186–190, https://doi.org/10.1016/j.mssp.2017.04.025.

[38] T. Seike, J. Nagai, Electrochromism of 3d transition metal oxides, Solar Energy Materials 22 (1991) 107–117, https://doi.org/10.1016/0165-1633(91)90010-i.

[39] K.H. Groh, H.W. Loeb, State of the art of radio-frequency ion sources for space propulsiona, Rev. Sci. Instrum. 65 (1994) 1741–1744, https://doi.org/10.1063/1.1144869.

[40] K. Holste, P. Dietz, S. Scharmann, K. Keil, T. Henning, D. Zschätzsch, M. Reitemeyer, B. Nauschütt, F. Kiefer, F. Kunze, J. Zorn, C. Heiliger, N. Joshi, U. Probst, R. Thüringer, C. Volkmar, D. Packan, S. Peterschmitt, K.-T. Brinkmann, H.-G. Zaunick, M.H. Thoma, M. Kretschmer, H.J. Leiter, S. Schippers, K. Hannemann, P.J. Klar, Ion thrusters for electric propulsion: scientific issues developing a niche technology into a game changer, Rev. Sci. Instrum. 91 (2020) 61101, https://doi.org/10.1063/5.0010134.

[41] R. Hippler, C. Denker, Generation of positively and negatively charged molecular ions during sputtering of a copper target by low-energy Ar + ion bombardment in a dilute argon/oxygen gas mixture, Plasma Sources Sci. Technol. 28 (2019) 35008, https://doi.org/10.1088/1361-6595/ab0706.

[42] M. Becker, P. Riedl, J. Kaupe, F. Michel, A. Polity, S. Mitić, Assessing a growth anomaly in ion-beam sputtered non-stoichiometric NiO x, J. Appl. Phys. 126 (2019) 134901, https://doi.org/10.1063/1.5116679.

[43] M. Becker, M. Gies, A. Polity, S. Chatterjee, P.J. Klar, Materials processing using radio-frequency ion-sources: ion-beam sputter-deposition and surface treatment, Rev. Sci. Instrum. 90 (2019) 23901, https://doi.org/10.1063/1.5063976.

[44] D. Kalanov, A. Anders, C. Bundesmann, Properties of secondary ions in ion beam sputtering of Ga2O3, J. Vac. Sci. Technol. A 39 (2021) 053409, https://doi.org/10.1116/6.0001204.

[45] D. Patel, Y. Wang, M. Larotonda, J. Lovewell, J. Jensen, K.J. Hsiao, E. Krous, J. J. Rocca, C.S. Menoni, F. Tomasel, S. Kholi, P. McCurdy, Assessing the impact of atomic oxygen in the damage threshold and stress of Hafnia films grown by ion beam sputter deposition, in: Laser-Induced Damage in Optical Materials: 2006, CO, SPIE, Boulder, 2006, p. 640314.

[46] M. Becker, J. Kessler, F. Kuhl, S.L. Benz, L. Chen, A. Polity, P.J. Klar, S. Chatterjee, Phase control of multivalent vanadium oxides VO x by ion-beam sputter-

deposition, Phys. Status Solidi A 219 (2022) 2100828, https://doi.org/10.1002/pssa.202100828.
[47] M. Gies, F. Michel, C. Lupó, D. Schlettwein, M. Becker, A. Polity, Electrochromic switching of tungsten oxide films grown by reactive ion-beam sputter deposition, J. Mater. Sci. 56 (2021) 615–628, https://doi.org/10.1007/s10853-020-05321-y.
[48] J.P. Lehan, R.B. Sargent, R.E. Klinger, High-rate aluminum oxide deposition by MetaModeTM reactive sputtering, J. Vac. Sci. Technol. A 10 (1992) 3401–3406, https://doi.org/10.1116/1.577791.
[49] D. Nečas, P. Klapetek, Gwyddion: an open-source software for SPM data analysis, Open Physics 10 (2012), https://doi.org/10.2478/s11534-011-0096-2.
[50] D.A. Shirley, High-resolution X-ray photoemission spectrum of the valence bands of gold, Phys. Rev. B 5 (1972) 4709–4714, https://doi.org/10.1103/physrevb.5.4709.
[51] A. Dulmaa, F.G. Cougnon, R. Dedoncker, D. Depla, On the grain size-thickness correlation for thin films, Acta Mater. 212 (2021) 116896, https://doi.org/10.1016/j.actamat.2021.116896.
[52] A. Bakin, J. Kioseoglou, B. Pecz, A. El-Shaer, A.-C. Mofor, J. Stoemenos, A. Waag, Misfit reduction by a spinel layer formed during the epitaxial growth of ZnO on sapphire using a MgO buffer layer, J. Cryst. Growth 308 (2007) 314–320, https://doi.org/10.1016/j.jcrysgro.2007.08.012.
[53] G. Greczynski, L. Hultman, X-ray photoelectron spectroscopy: towards reliable binding energy referencing, Prog. Mater. Sci. 107 (2020) 100591, https://doi.org/10.1016/j.pmatsci.2019.100591.
[54] M.C. Biesinger, B.P. Payne, L.W.M. Lau, A. Gerson, R.C. St, Smart, X-ray photoelectron spectroscopic chemical state quantification of mixed nickel metal, oxide and hydroxide systems, Surf. Interface Anal. 41 (2009) 324–332, https://doi.org/10.1002/sia.3026.
[55] K.S. Kim, N. Winograd, X-ray photoelectron spectroscopic studies of nickel-oxygen surfaces using oxygen and argon ion-bombardment, Surf. Sci. 43 (1974) 625–643, https://doi.org/10.1016/0039-6028(74)90281-7.
[56] A.N. Mansour, Characterization of NiO by XPS, Surf. Sci. Spectra 3 (1994) 231–238, https://doi.org/10.1116/1.1247751.
[57] H.W. Nesbitt, D. Legrand, G.M. Bancroft, Interpretation of Ni2p XPS spectra of Ni conductors and Ni insulators, Phys. Chem. Miner. 27 (2000) 357–366, https://doi.org/10.1007/s002690050265.
[58] C. Bundesmann, A. Hellmich, Energy distributions of secondary ions for the Ar ion beam sputtering of indium tin oxide, Journal of Vacuum Science & Technology B, Nanotechnology and Microelectronics: Materials, Processing, Measurement, and Phenomena 38 (2020) 064002, https://doi.org/10.1116/6.0000516.
[59] G. Wulff, XXV. Zur Frage der Geschwindigkeit des Wachsthums und der Auflösung der Krystallflächen, Zeitschrift für Kristallographie, Crystalline Materials 34 (1901) 449–530, https://doi.org/10.1524/zkri.1901.34.1.449.
[60] L.D. Marks, L. Peng, Nanoparticle shape, thermodynamics and kinetics, J. Phys. Condens. Matter 28 (2016) 53001, https://doi.org/10.1088/0953-8984/28/5/053001.
[61] R. Kužel, L. Nichtová, Z. Matěj, J. Musil, In-situ X-ray diffraction studies of time and thickness dependence of crystallization of amorphous TiO2 thin films and stress evolution, Thin Solid Films 519 (2010) 1649–1654, https://doi.org/10.1016/j.tsf.2010.08.122.
[62] S.K. Kim, S. Hoffmann-Eifert, M. Reiners, R. Waser, Relation between enhancement in growth and thickness-dependent crystallization in ALD TiO[sub 2] thin films, J. Electrochem. Soc. 158 (2011) D6, https://doi.org/10.1149/1.3507258.
[63] P. Ravikumar, D. Taparia, P. Alagarsamy, Thickness-dependent thermal oxidation of Ni into NiO thin films, J. Supercond. Nov. Magn. 31 (2018) 3761–3775, https://doi.org/10.1007/s10948-018-4651-6.
[64] A. Vahl, J. Dittmann, J. Jetter, S. Veziroglu, S. Shree, N. Ababii, O. Lupan, O. C. Aktas, T. Strunskus, E. Quandt, R. Adelung, S.K. Sharma, F. Faupel, The impact of O2/Ar ratio on morphology and functional properties in reactive sputtering of metal oxide thin films, Nanotechnology 30 (2019) 235603, https://doi.org/10.1088/1361-6528/ab0837.
[65] D. Brassard, D.K. Sarkar, M.A. El Khakani, L. Ouellet, High- k titanium silicate thin films grown by reactive magnetron sputtering for complementary metal–oxide–semiconductor applications, J. Vac. Sci. Technol. A 22 (2004) 851–855, https://doi.org/10.1116/1.1722530.
[66] E.L. Miller, D. Paluselli, B. Marsen, R.E. Rocheleau, Development of reactively sputtered metal oxide films for hydrogen-producing hybrid multijunction photoelectrodes, Sol. Energy Mater. Sol. Cells 88 (2005) 131–144, https://doi.org/10.1016/j.solmat.2004.07.058.
[67] N. Matsunami, Y. Yamamura, Y. Itikawa, N. Itoh, Y. Kazumata, S. Miyagawa, K. Morita, R. Shimizu, H. Tawara, Energy dependence of the ion-induced sputtering yields of monatomic solids, At. Data Nucl. Data Tables 31 (1984) 1–80, https://doi.org/10.1016/0092-640X(84)90016-0.
[68] M.N. Mitsuhiro Nagashima, S.N. Shin-ichi Nakano, K.S. Kimihiro Sasaki, T. H. Tomonobu Hata, Growth dependence of reactively sputtered yttria-stabilized zirconia on Si(100), (110), (111) substrates, Jpn. J. Appl. Phys. 38 (1999) L74, https://doi.org/10.1143/jjap.38.l74.
[69] C. Bundesmann, C. Eichhorn, H. Neumann, F. Scholze, D. Spemann, M. Tartz, H. J. Leiter, R.Y. Gnizdor, F. Scortecci, In situ erosion measurement tools for electric propulsion thrusters: triangular laser head and telemicroscope, EPJ Techn Instrum 9 (2022), https://doi.org/10.1140/epjti/s40485-022-00076-z.